Intrinsically shaping the focal behavior with multi-ring Bessel-Gaussian beam

H. Ye, , K. Huang, , H. Liu, , F. Wen, , Z. Jin, , J. Teng, and , and C.-W. Qiu

Citation: Appl. Phys. Lett. **111**, 031103 (2017); doi: 10.1063/1.4986498
View online: http://dx.doi.org/10.1063/1.4986498
View Table of Contents: http://aip.scitation.org/toc/apl/111/3
Published by the American Institute of Physics

Intrinsically shaping the focal behavior with multi-ring Bessel-Gaussian beam

H. Ye,[1,a)] K. Huang,[2,a)] H. Liu,[2] F. Wen,[1,3] Z. Jin,[1] J. Teng,[2,b)] and C.-W. Qiu[1,b)]
[1]*Department of Electrical and Computer Engineering, National University of Singapore, 4 Engineering Drive 3, Singapore 117576*
[2]*Institute of Materials Research and Engineering, Agency for Science, Technology and Research (A*STAR), 3 Research Link, Singapore 117602*
[3]*Key Laboratory for Physical Electronics and Devices of the Ministry of Education & Institute of Wide Bandgap Semiconductors, Xi'an Jiaotong University, Xi'an 710049, China*

(Received 5 June 2017; accepted 3 July 2017; published online 17 July 2017)

Traditional manipulation of light generally employs diffractive optical elements such as binary phase or amplitude masks. However, we have found that vector Bessel-Gaussian (BG) beams have the intrinsic capacity of forming a special intensity pattern without additional optical elements. Using the vector diffraction theory, we theoretically show that several optical patterns (e.g., hollow beam, bottle beam, optical needle, and spot) can be created only by dynamically tailoring vector BG beams through their beam parameters (viz., polarization order n, transverse wave number β, and beam waist w_0). These results yield a useful guideline for the adjustable beam parameter to generate a certain optical pattern in the focal region. The proposed roadmap of manipulating the structured beams by their intrinsic properties might open an alternative avenue for beam shaping. *Published by AIP Publishing*. [http://dx.doi.org/10.1063/1.4986498]

Light focusing is the fundamental feature of numerous applications, ranging from optical microscopy, lithography, optical data storage, material processing to optical trapping and manipulation.[1–6] In principle, the polarization properties of the incident beam play an important role in determining the size, shape, and polarization of the focal field; for instance, a highly focused laser beam creates distinct features on materials depending on the handedness and spatial polarization of the laser beam, thus leading to direct laser-machined structures on a subwavelength scale.[1,4,5] Moreover, the spatial intensity distribution at the entrance pupil of the focusing lens also notably affects the field near the focus. One of the prominent examples is the scanning microscope based on the flat lens where the central region is opaque, which helps to produce a deep subwavelength needle with long focal depth and allows for mapping the horizontal details of a 3D object with a rugged surface.[3]

In general, directly focusing of the laser beam usually leads to limited optical patterns with a full width at half maximum (FWHM) above the diffraction limit[1] and short focal depth,[7] especially for the light with the spatially homogeneous polarization and intensity profile. Therefore, diffractive optical elements (DOEs), which introduce the appropriate phase or amplitude modulation, are widely employed in beam shaping. The spatial light modulator (SLM) is one of the most common devices for phase and amplitude modulation.[8,9] However, constrained by the micron-sized pixel size of SLM, beam shaping at the wavelength scale is unattainable by using SLM.[8–10] Moreover, nanostructured metalens and diffractive optical elements (DOEs) have also been extensively investigated for light focusing on a subwavelength scale.[2,3,7] Nevertheless, beam shaping based on metalens and DOEs requires intricate design and precise fabrication of additional nanostructures, which incur high costs in time and resources. Hence, beam manipulation via directly focusing the laser beam without fabricating additional optical elements will be of great interest in various applications.

A vector beam with Bessel-Gaussian (BG) distribution, which can be experimentally generated via many existing approaches,[11,12] has been approved to be one of the vector solutions to the Helmholtz equation under the paraxial approximation.[13] Its properties such as amplitude and polarization profiles can be tuned by modifying its order n, transverse wave number β, and beam waist w_0. Naturally, a phase difference π between neighboring rings inherently exists in vector multi-ring-shaped (MRS) BG beams. Hence, such a MRS beam with its distinctive phase and amplitude modulation offers exceptional benefits for beam shaping. This offers an inartificial approach to realize both fabrication-free and dynamic engineering properties during the generation of several optical patterns. In this letter, an efficient approach to experimentally generate vector BG beams is demonstrated. We employ the vector diffraction theory to study beam manipulation via tuning n, β, and w_0 of vector BG beams. It is illustrated that a bottle-hollow or bottle beam[14,15] and focal spot can be produced by directly focusing the BG beam. Moreover, a subwavelength optical needle can also be generated by properly choosing the beam parameters. The map describing the focusing properties of the vector BG beams provides a complete illustration of the optical patterns in the focal region. This efficient beam shaping approach enabled by focusing vector BG beams may find applications for optical manipulation both in physics and biology.

For the convenience of studying cylindrical vector (CV) beams with rotational symmetry, the electric field of cylindrical vector beams can be expressed in a cylindrical coordinate

[a)]H. Ye and K. Huang contributed equally to this work.
[b)]Electronic addresses: jh-teng@imre.a-star.edu.sg and eleqc@nus.edu.sg.

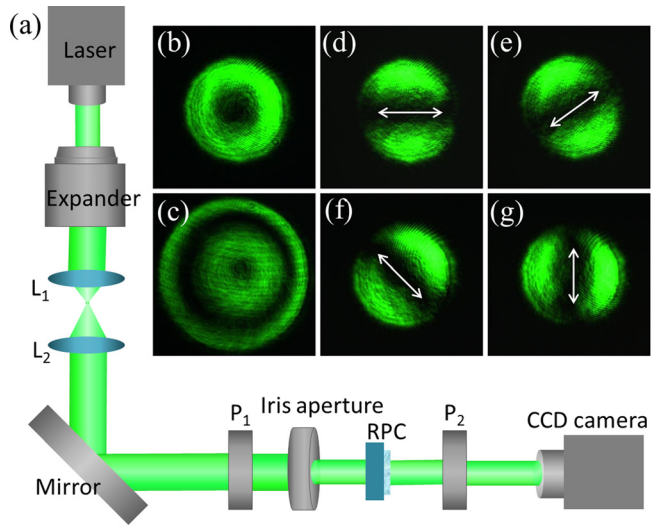

FIG. 1. Generation and optical characterization of the CV beam. (a) Schematic of the experimental setup. L_1 and L_2: lens, P_1 and P_2: linear polarizer, and RPC: radial polarization converter. (b) and (c) Experimentally recorded intensity distributions. (d)–(g) The intensity patterns of the CV beam after being filtered by P_2 at different angles. The white arrows indicate the orientations of the polarizer.

$$\vec{E}(r,\varphi,z') = A(r,z')\{[\cos(\mathrm{n}-1)\varphi+\varphi_0]\vec{e}_r + [\sin(n-1)\varphi+\varphi_0]\vec{e}_\varphi\}, \quad (1)$$

where the polarization order n is an integer, φ_0 is the initial polarization angle and taken as zero in this letter, and $A(r,z')$ is the amplitude factor.[11] At $z'=0$, we have $A(r,0)=\exp(-r^2/w_0^2)J_n(\beta r)$, where w_0 is the waist radius, β is the transverse wave number determining the beam profile, and J_n is the n-order Bessel function of the first kind. Figure 1(a) schematically depicts the experimental setup to generate CV beams. A laser beam ($\lambda=532\,\mathrm{nm}$) with linear polarization is first expanded and collimated. The resulting light with linear polarization is then converted to a CV beam by using a radial polarization converter (RPC);[16] meanwhile, the beam width can be dynamically controlled by the iris aperture. The far-field radiation patterns of the vector CV beam are experimentally recorded by using the charge-coupled device (CCD) and illustrated in Figs. 1(b) and 1(c), where single-ring-shaped (SRS) and MRS beams with good rotational symmetry are presented. In order to reveal its polarization status, another linear polarizer P_2 is employed in the experiment. By rotating P_2, the optical fields under different rotating angles are recorded by using the CCD and displayed in Figs. 1(d)–1(g), which help to identify the radial polarization. Although only beams with one and two rings are depicted here, CV beams with different rings can be generated with the same setup by tuning the iris aperture. It differs from the traditional methods based on the metasurface where the output beam is settled once the device has been fabricated.[2,3]

In order to further illustrate the properties of the CV beam, Figs. 2(a)–2(c) display the polarization and intensity profiles of the vector beam for $n=-1$, 1, and 2, respectively. As one kind of vector vortex beam containing the spin and orbital angular momenta,[13,17] the CV beam has an annular intensity distribution in the transverse plane, where the dark region at the center denotes a polarization singularity. The topological charge of the CV beam can be illustrated via the arm number of spirals generated by the interference with a co-propagating spherical beam, as shown in Figs. 2(d)–2(f). A π phase difference is identified between the adjacent rings as shown in Figs. 2(a)–2(c). Conventionally, the binary phase mask should be introduced to generate a π phase difference to make constructive or destructive interference occur in the desired region.[7,15] However, the CV beam comes very naturally with unique phase properties, i.e., two neighboring rings having the phase difference of π. Moreover, we observe that the intensity in the innermost ring of the MRS beam is the strongest, whereas it decreases rapidly in the rings further away from the beam center. Hence, such a MRS beam with its distinctive phase and amplitude modulation offers exceptional benefits for beam shaping by tuning its intrinsic properties such as n, w_0, and β.

Based on the distinct properties of the MRS beam introduced above, it is interesting to study how the intrinsic

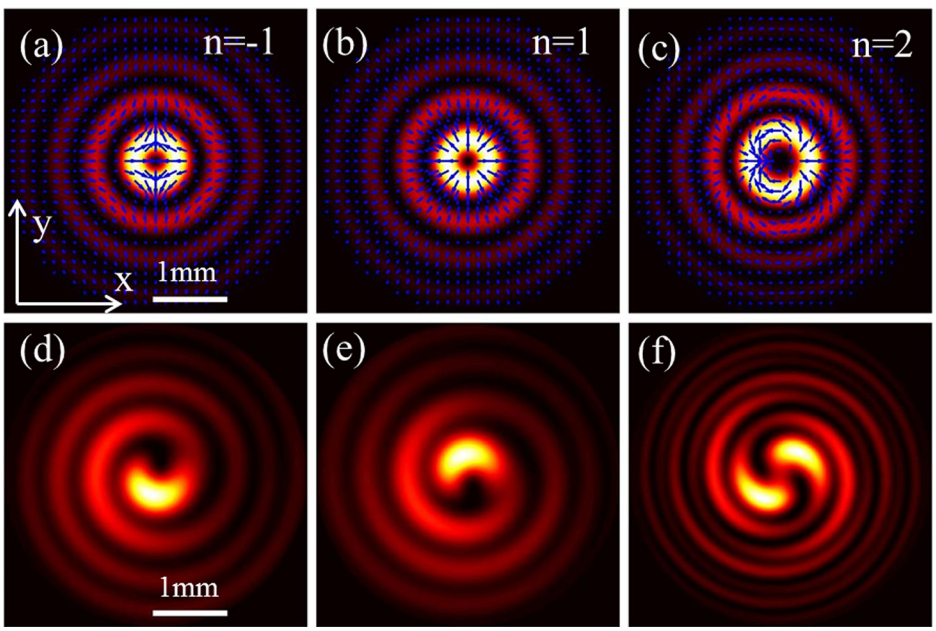

FIG. 2. Simulated polarization status and intensity distributions of the MRS beam ($\beta=6\,\mathrm{mm}^{-1}$ and $w_0=2.5\,\mathrm{mm}$). (a) n = –1, (b) n = 1, and (c) n = 2. The polarization status of the beam is indicated by the blue arrows. (d)–(f) Simulated interference patterns of the MRS beams and co-propagating spherical beam shown in (a), (b), and (c), respectively.

phase and amplitude modulation will affect its focusing properties. Figure 3(a) illustrates the schematic of focusing the BG beam with a high numerical-aperture (NA) lens. Various optical patterns (e.g., optical null field, needle, and hotspot) are expected to be generated in the focal region. According to Richards and Wolf's theory,[18] the vector fields in the focal region can be written as

$$E_\rho(r,\varphi,z) = Ci^{n+1}\cos[(n-1)\varphi+\varphi_0]\int_0^\alpha P(\theta)A(\theta) \times [\cos\theta(J_n - J_{n-2}) + (J_n + J_{n-2})]\sin\theta e^{ikz\cos\theta}d\theta, \tag{2}$$

$$E_\varphi(r,\varphi,z) = Ci^{n+1}\sin[(n-1)\varphi+\varphi_0]\int_0^\alpha P(\theta)A(\theta) \times [\cos\theta(J_n + J_{n-2}) + (J_n - J_{n-2})]\sin\theta e^{ikz\cos\theta}d\theta, \tag{3}$$

$$E_z(r,\varphi,z) = -2Ci^{n}\cos[(n-1)\varphi+\varphi_0]\int_0^\alpha P(\theta)A(\theta) \times J_{n-1}\sin^2\theta e^{ikz\cos\theta}d\theta, \tag{4}$$

where $A(\theta) = (\cos\theta)^{-3/2}$ is the apodization factor of the aplanatic lens,[1,13] C is a constant, $\sin\alpha = NA$, and $J_m = J_m(kr\sin\theta)$. The pupil function of the incident beam is $P(\theta) = \exp(-\gamma^2\frac{\tan^2\theta}{\tan^2\alpha})J_n(\beta\omega_0\gamma\frac{\tan\theta}{\tan\alpha})$, where γ is the ratio of the pupil radius and the beam waist w_0 is assumed to be unity. Let us start with vector BG beams with $\beta = 6\,\mathrm{mm}^{-1}$ and w_0=2.5 mm, whose intensity profiles and polarization status are displayed in Figs. 2(a)–2(c). From the simulation results obtained from Eqs. (2)–(4), it can be found that the focused BG beam with n ≠ 1 results in asymmetric beams at the focus due to the complex polarization states of the incidence (see Fig. S1 in the supplementary material). In contrast, the vector BG beam with n = 1 leads to a symmetric light field. Mathematically, Eq. (1) reduces to the well-known radially polarized CV beam when n = 1. It is well known that the SRS radially polarized CV beam results in a sharp hotspot with a strong longitudinal component if directly focused by a high-NA lens.[19] However, it is found that focused MRS beams also lead to a bottle-shape beam. Hence, it is of vital importance to fully study the focusing properties of the vector CV beams with different n, w_0, and β values. In this study, we restrict our studies to the vector BG beam with n = 1, as rotational symmetry is highly desired in many practical applications.

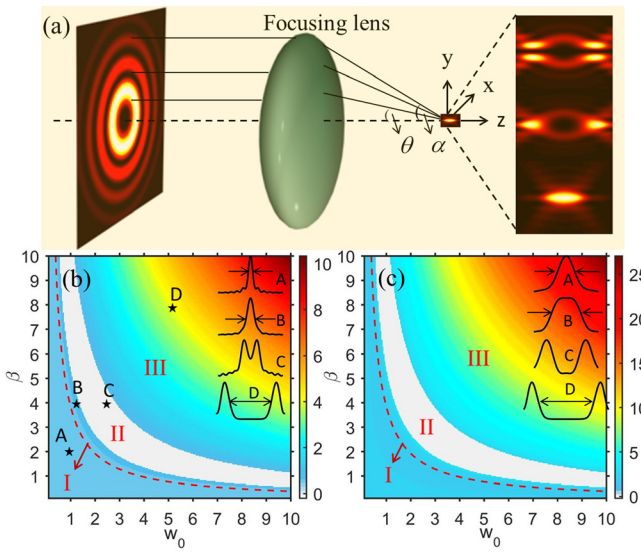

FIG. 3. (a) The schematic of focusing the MRS Bessel-Gaussian beam with a high-NA lens. Variety field patterns are expected to be generated in the focal region. (b) FWHM along the radial direction. (c) FWHM along the optical axis. Points A, B, C, and D (marked by stars) represent four CV beams, and their field intensity distributions along the radial direction and the optical axis are plotted at the top right corner. The red dashed curve represents the line $w_0\beta = 3.834$, which is the first solution of the first order Bessel function of the first kind.

Before we study the focusing properties of the SRS beam and the MRS beam, it is necessary to mathematically differentiate SRS and MRS beams. According to the first solution of the 1-order Bessel function of the first kind, we can calculate and demarcate the regions (w_0 and β) of the SRS and MRS beams. As shown in Figs. 3(b) and 3(c), these regions are separated by the red-dashed line: the area below the red-dashed line is the region where the SRS beam exists, whereas the other regions are for MRS beams. Figure 3(b) also presents the FWHM (in units of λ) of the null field or hotspot along the radial direction at the focal plane (x-y plane) as a function of w_0 and β. As examples, the field intensity distributions along the lateral direction at points A (where w_0=1.05 and $\beta = 2$), B (where w_0=1.31 and $\beta = 4$), C (where w_0=2.5 and $\beta = 4$), and D (where w_0=5 and $\beta = 8$) are plotted at the top right corner (see Fig. S2 in the supplementary material for the properties of ABCD). For each point in Fig. 3(b), the field intensity along the radial direction is first normalized to the maximum; then, the values of the FWHM at these points are measured at half maximum. It can be inferred that the fields at points A and B are hotspots, while there is a null field at point D. It should be addressed that the FWHM at point C is not included in our study as w_0 and β at this point will lead to saddle-shaped distribution, which is beyond the scope of interest here.

In addition to the selected points A, B, C, and D in Fig. 3(b), it can also be observed that the values of the FWHM change progressively in accordance with w_0 and β. From the colorbar in Fig. 3(b), we note that the FWHM of the hotspot at the focus in some regions of I is at the subwavelength scale. Obviously, the subwavelength hotspot achieved with this mechanism differs from the spot obtained with super-oscillatory lens having a smaller hotspot at the cost of high-intensity sidelobes.[20] Nevertheless, there is a white region II where the choice of w_0 and β gives rise to a focal field with saddle-shaped distribution which is neither a hot spot nor the optical null field. It is obvious that Fig. 3(b), which presents the focusing properties of vector BG beams with various w_0 and β values, can serve as a full guideline for choosing BG beams in real applications. Instead of exchanging the focusing lens or designing another mask,[5] our scheme unambiguously shows that the pattern of the focused spot can alternately be varied by tuning the profiles of the incident light.

Furthermore, the axial performance of the focused vector BG beams is also presented in Fig. 3(c). The field intensity profiles along the optical axis at points A, B, C, and D are also plotted at the top right corner for showing their differences. It

is evident that the focused BG beam at point A has a Gaussian on-axis distribution similar to its lateral or transverse intensity. At point B, however, the on-axis intensity has a flat top shape, which differs from a hotspot in Fig. 3(b); this implies that BG beams in this region can lead to a subwavelength needle that means a long focal depth and uniform axial intensity distribution without resorting to conventional phase or amplitude masks.[21] In order to clearly show the properties of the focal field, the field intensity distributions of the optical needle along x-y and y-z planes are depicted in Figs. 4(c) and 4(d). Meanwhile, the field intensity of the hotpot in the x-y plane is plotted in Fig. 4(e). According to the FWHM of the needle and hotspot along radial and axial directions [Fig. 4(f)], the FWHM of the focal spot is estimated as 0.47λ. The axial and radial FWHMs of the needle are 3.02λ and 0.75λ, respectively. This kind of needle may benefit many applications which require a long depth of focus.[3] Similar to Fig. 3(b), a white region II and another two regions (I and III) which correspond to those marked in Fig. 3(b) are also identified in Fig. 3(c). It should be further emphasized that the longitudinal FWHM along the optical axis is larger than the lateral one. Usually, the lateral resolution in microscopy is proportional to $1/NA$, while the axial resolution is proportional to $1/NA^2$.[6,15] According to Ref. 15, a similar mechanism can be applied to tune the size of the optical pattern by exchanging the NA of the focusing lens. In the case of the MRS beam, the focal field is a bottle beam when focused by high-NA lens, as shown in Fig. 4(a). However, if the NA of the lens is small, for example, 0.01 in Fig. 4(b), the focal field turns into a bottle-hollow beam with a length on the scale of mm.

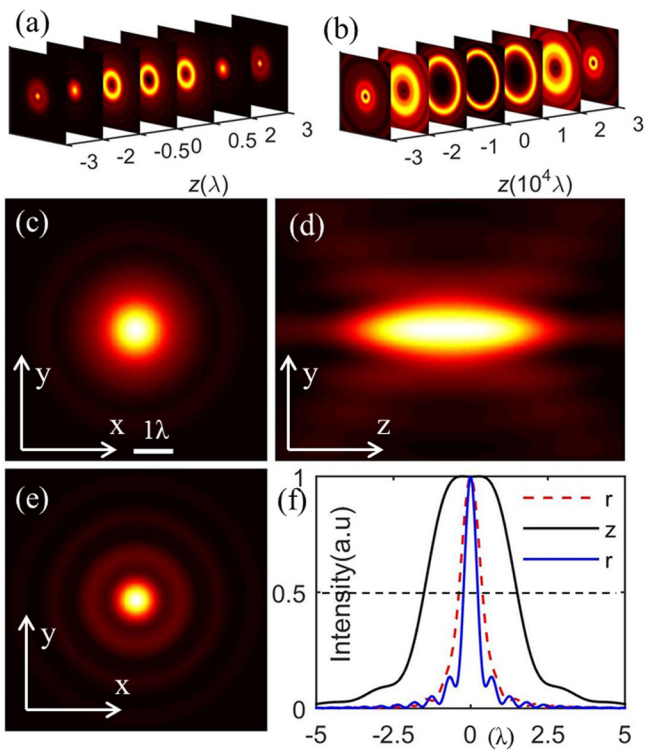

FIG. 4. Different focal patterns are generated by focusing the BG beam. A bottle beam (a) and a hollow-bottle beam (b) are created by focusing the BG beams with parameters shown in Figs. 2(b) and 2(a), respectively. (c) and (d) Field intensity distributions of the optical needle. (e) Field intensity distribution of a subwavelength spot. (f) The FWHM of the needle and spot along radial and axial directions.

Combining the results in Figs. 3 and 4, we can infer the following about the focusing properties of various vector BG beams:

- For a SRS beam (e.g., point A), its focused pattern at the focal plane always leads to a hotspot. The subwavelength hotspot can be obtained by properly tuning the beam waist and transverse wave number.
- For the MRS beams with parameters located in region I (e.g., point B), an optical needle with uniform axial intensity distribution and subwavelength lateral size can be obtained.
- For the MRS beams with parameters located in the white region II (e.g., point C), a saddle-shaped intensity profile lying between the needle and the null field is generated.
- For the MRS beams with parameters located in region III, which contain a vast majority of all the vector BG beams, each of their optical patterns in the focal region yields a null field as shown in Fig. 3.

In summary, we have employed the vector diffraction theory to study beam shaping by focusing vector Bessel-Gaussian beams with different topological charge n, transverse wave number β, and beam waist w_0. We have shown that the bottle-hollow beam, bottle beam, and focal spot can be created by dynamically engineering vector Bessel-Gaussian beams. A subwavelength optical needle can also be generated by properly choosing the beam parameters. The map describing the focusing properties of the vector Bessel-Gaussian beams provides a complete illustration of the optical pattern in the focal region. The proposed scheme of directly focusing the vector beams without fabricating additional optical elements may find interesting applications both in physics and biology.

See supplementary material for the focusing properties of vector BG beams with different n, the intensity profiles, and focusing properties of BG beams at ABCD.

This work was financially supported by the A*STAR BEP Grant No. 1521480031.

[1]Q. Zhan, Adv. Opt. Photonics **1**(1), 1 (2009).
[2]M. Khorasaninejad, W. Chen, R. C. Devlin, J. Oh, A. Y. Zhu, and F. Capasso, Science **352**(6290), 1190 (2016).
[3]F. Qin, K. Huang, J. Wu, J. Teng, C. Qiu, and M. Hong, Adv. Mater. **29**(8), 1602721 (2017).
[4]C. Hnatovsky, V. Shvedov, N. Shostka, A. Rode, and W. Krolikowski, Opt. Lett. **37**(2), 226 (2012).
[5]C. Hnatovsky, V. Shvedov, W. Krolikowski, and A. Rode, Phys. Rev. Lett. **106**(12), 123901 (2011).
[6]V. G. Shvedov, A. V. Rode, Y. V. Izdebskaya, A. S. Desyatnikov, W. Krolikowski, and Y. S. Kivshar, Phy. Rev. Lett. **105**(11), 118103 (2010).
[7]H. Wang, L. Shi, B. Luk'yanchuk, C. J. R. Sheppard, and C. T. Chong, Nat. Photonics **2**(8), 501 (2008).
[8]F. K. Fatemi and M. Bashkansky, Opt. Lett. **31**(11), 864 (2006).
[9]N. Matsumoto, T. Inoue, T. Ando, Y. Takiguchi, Y. Ohtake, and H. Toyoda, Opt. Lett. **37**(15), 3135 (2012).
[10]D. J. McKnight, K. M. Johnson, and R. A. Serati, Appl. Opt. **33**(14), 2775 (1994).
[11]A. Hakola, S. C. Buchter, T. Kajava, H. Elfström, J. Simonen, P. Pääkkönen, and J. Turunen, Opt. Commun. **238**(4), 335 (2004).
[12]R. Takeuchi, Y. Kozawa, and S. Sato, J. Opt. **15**(7), 075710 (2013).
[13]K. Huang, P. Shi, G. W. Cao, K. Li, X. B. Zhang, and Y. P. Li, Opt. Lett. **36**(6), 888–890 (2011).
[14]I. Epstein and A. Arie, Opt. Lett. **39**(11), 3165 (2014).
[15]H. Ye, C. Wan, K. Huang, T. Han, J. Teng, S. P. Yeo, and C.-W. Qiu, Opt. Lett. **39**(18), 630 (2014).

[16]M. Beresna, M. Gecevičius, and P. G. Kazansky, Opt. Mater. Express **1**(4), 783 (2011).
[17]H. Wu, J. Tang, Z. Yu, J. Yi, S. Chen, J. Xiao, C. Zhao, Y. Li, L. Chen, and S. Wen, Opt. Commun. **393**, 49 (2017).
[18]B. Richards and E. Wolf, Proc. R. Soc. London, Ser. A **253**(1274), 358 (1959).
[19]R. Dorn, S. Quabis, and G. Leuchs, Phys. Rev. Lett. **91**, 233901 (2003).
[20]K. Huang, H. Ye, J. Teng, S. P. Yeo, B. Luk'yanchuk, and C.-W. Qiu, Laser Photonics Rev. **8**(1), 152 (2014).
[21]H. Ye, C.-W. Qiu, K. Huang, J. Teng, B. Luk'yanchuk, and S. P. Yeo, Laser Phys. Lett. **10**(6), 065004 (2013).